



# Preparation of porous diethylene triamine reduced graphene oxide aerogel for efficient pollutant dye adsorption

Leilei Jiang<sup>1</sup> · Xuebing Hu<sup>1</sup> · Boshen Yang<sup>1</sup> · Zhiyong Yang<sup>1</sup> · Chuanbiao Lu<sup>1</sup>

Accepted: 17 February 2023 / Published online: 5 March 2023

© The Author(s), under exclusive licence to Springer Science+Business Media, LLC, part of Springer Nature 2023

## Abstract

Diethylene triamine (DETA) reduced graphene oxide aerogel (DRA) was fabricated by self-assembly and freeze-drying method. The effects of preparation processes, including reduction temperature and DETA concentration, on the aerogel performance were investigated. It can be found that the density of the as-prepared DRA-8 is as low as 11.15 mg/cm<sup>3</sup> when the DETA concentration is 16 μL/mL, and the reduction temperature is 95 °C. And the DRA-8 has abundant macro-pores between 10 and 100 μm in size. Meanwhile, using azo dyes as adsorbates, the adsorption capacities of DRA-8 under different process conditions were examined. The results demonstrate that the pseudo-second-order model and the Langmuir isotherm model agree well with the experimental data. At 298 K, the adsorption capacities for methyl orange (MO) and methylene blue (MB) are up to 227.24 and 266.82 mg/g, respectively. The thermodynamics analysis presents the adsorption belongs to a spontaneous thermodynamic reaction. The adsorption mechanism of DRA-8 for MO and MB was also explained. Meantime, DRA-8 can have a high adsorption capacity for MB and MO after multiple cycles. All of these point to the possibility of using DRA-8 as a suitable adsorbent material for dye elimination from aqueous environments.

**Keywords** Reduced graphene oxide aerogel · Diethylene triamine · Azo dye · Adsorption capacity

## 1 Introduction

Water pollution caused by organic dyes is currently one of the concerned serious environmental issues in many countries. The global annual production of dyes exceeds 700,000 tons, and about 10–15% of these dyes will be discharged into the aquatic environment [1, 2]. Since the dyes in wastewater are very difficult to degrade, they will remain in the human body and combine with biological cells, thus posing a severe threat to aquatic organisms and human beings [3]. Consequently, it is of great significance and urgency to remove dyes from water. Up to now, the dye removal methods mainly include adsorption, ion exchange, membrane filtration, electrochemical degradation, photocatalytic degradation and biological treatment [4, 5]. Among these methods, adsorption has been extensively utilized due to its benefits of easy handling, reduced energy consumption, and low cost [6]. However, traditional adsorption materials, such

as activated carbon, silica gel, bentonite, zeolite and diatomaceous earth, especially powdered adsorbents, are likely to cause secondary pollution, and the adsorption capacity still needs to be improved. Therefore, developing new high-efficiency adsorption materials is imminent [7].

As a 2D matter, graphene oxide (GO) has amazing application prospects in adsorption thanks to its huge specific surface area, plentiful groups and easy modification [8, 9]. Meanwhile, since GO is easy to disperse in water, it as an adsorbent will be challenging to sediment and separate from water following adsorption, thus easily causing secondary pollution. To solve this problem, functionalizing GO and assembling it into a three-dimensional block aerogel will not only retain its excellent adsorption characteristics, but also achieve rapid and efficient separation from water after adsorption. Recently, Singh used polylysine as a crosslinker and nitrogen dopant to prepare a functionalized graphene aerogel. The aerogel shown a high adsorption capacity for Cr(VI) [10]. Trinh utilized ethylenediamine to reduce GO and obtained the graphene aerogel material. With amino modification, its adsorption capacities for azo dyes (MB and MO) were 221.74 and 166.67 mg/g, respectively [11]. Chen used cysteamine

✉ Xuebing Hu  
xuebinghu2010@gmail.com

<sup>1</sup> Key Laboratory of Inorganic Membrane, Jingdezhen Ceramic Institute, Jingdezhen 333001, China

to crosslink GO nanosheets by a one-step hydrothermal synthesis method to obtain the cross-linked GO aerogel. With sulfhydryl and amino modifications, its adsorption capacities for MB and MO were 207.8 and 70.2 mg/g, respectively [12]. Tang prepared graphene aerogel with polyvinyl alcohol as a crosslinking agent. The adsorption capacities of the aerogel for MB, MO, malachite green, and Rhodamine B were 88 mg/g, 21 mg/g, 352 mg/g, and 139 mg/g, respectively [13].

However, the above works still have some shortcomings that limit the application of functionalized graphene aerogels, such as the reducing agent or cross-linking agent is less safe or expensive, and the dye adsorption capacity of aerogel products needs to be improved. Although urea has been widely used as a low-cost reducing agent, it is unstable and lacks available cross-linking effect in the preparation of functionalized graphene aerogels. Therefore, it is crucial to develop a new reducing/cross-linking agent to prepare high-performance functionalized graphene aerogel materials.

Herein, we utilized a mild and cheap diethylene triamine (DETA) as a reducing/cross-linking agent to prepare a novel high-performance reduced graphene oxide aerogel at a lower temperature. The as-prepared aerogel possesses the advantages of low density, plentiful pore structure and outstanding adsorption capacity for the organic dyes (anionic MO and cationic MB) in water. Our work provides a competitive adsorption material to solve the growing problem of dye contamination in the aquatic environment.

## 2 Experimental

### 2.1 Materials

Graphite powder (99.5%) was bought from Aladdin Biochemical Technology Co. Ltd. Diethylene triamine (DETA,  $C_4H_{13}N_3$ ), sodium hydroxide, concentrated hydrochloric acid (35%), methylene blue trihydrate (MB,  $C_{16}H_{18}ClN_3S \cdot 3H_2O$ ) and methyl orange (MO,  $C_{14}H_{14}N_3SO_3Na$ ) were bought from Sinopharm Chemical Reagent Co., Ltd.

### 2.2 Preparation of DRA

The GO synthesis process was described in detail in our earlier report [14]. DRA was prepared by chemical reduction at a lower temperature, and the preparation process is shown in Fig. 1. Briefly, 25 mL of 4 mg/mL GO suspension was mixed with a certain amount of DETA and stirred. Then the mixture was moved to a high-pressure Teflon reactor and reacted at a specific temperature for 16 h to obtain DETA reduced graphene oxide hydrogel (RGH). Next, the RGH was immersed in a 25% (V/V) aqueous ethanol solution to remove impurities. Finally, the RGH was frozen at  $-50\text{ }^\circ\text{C}$  and less than 10 Pa in a 10 N-50 A lyophilizer (Shuangjia Instrument Co. Ltd., China). After 24 h, the sample was moved from the freezer to a vacuum chamber for drying for 48 h to obtain the DRA products. All the above-mentioned parameters had been optimized by our early experiments.

In our experiment, the hydrogel samples prepared with DETA concentrations of 20  $\mu\text{L/mL}$  and at different reduction temperatures of 65, 75, 85 and 95  $^\circ\text{C}$  were labeled as

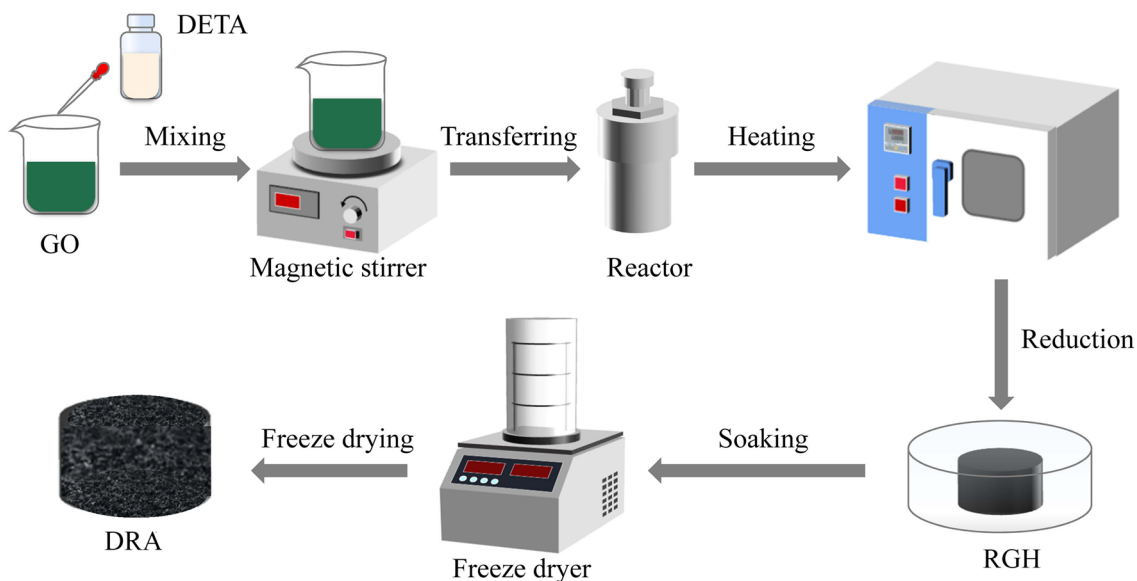


Fig. 1 Preparation process of DRA

RGH-1, RGH-2, RGH-3, and RGH-4, respectively. The aerogel samples prepared at different reduction temperatures of 65, 75, 85 and 95 °C were sequentially labeled from DRA-1 to DRA-4. The aerogel samples prepared with different DETA concentrations of 4, 8, 12, 16 and 24 μL/mL were sequentially labeled from DRA-5 to DRA-9.

### 2.3 Characterization

X-ray diffraction (XRD, D8 Advance, Germany) was utilized to analyze the samples. The defect characteristics of samples were determined using a laser Raman spectrometer (Thermo Scientific, Madison, USA). The group compositions of samples were observed by Fourier transform infrared spectroscopy (FTIR, Nicolet 5700, Thermo Fisher, USA). The morphology of sample was determined by scanning electron microscopy (SEM, Hitachi SU8220, Japan). The Zeta potentials of sample were characterized by Zeta potential analyzer (Zetasizer Nano, Malvern, UK). Analytical balance (ATX224R, SHIMADZU, Japan) and digital caliper were used to calculate the weights and dimensions of the materials, respectively. The bulk density was calculated from the mass-to-volume ratio of the sample.

### 2.4 Dye adsorption

In the adsorption experiments, the influences of temperature (298 K, 308 K, and 318 K), adsorption time (15–1200 min), starting concentration (50–250 mg/L) and pH value (4–10) on the adsorption capacity of DRA were explored. UV–visible spectrophotometer (UV-1601, Rayleigh Analysis Instrument Company, China) was used to determine the dye concentration in the solution. The pH value was altered via 0.1 M hydrochloric acid and sodium hydroxide. During the experiments, 15 mg DRA was immersed into 50 mL of different dye solutions respectively and continuously stirred for a period of time with a stirring velocity of 200 r/min.

The following is the equation for the adsorption amount ( $Q_t$ ) [15].

$$Q_t = (C_{\text{before}} - C_{\text{after}})V/m \quad (1)$$

$C_{\text{before}}$  and  $C_{\text{after}}$  are dye concentrations prior to and following adsorption (mg/L),  $V$  is the dye solution volume (mL), and  $m$  is the adsorbent mass (mg).

The different models were utilized to investigate the adsorption kinetics (Eqs. 2–4) [16–18].

$$\ln(Q_e - Q_t) = \ln Q_e - K_1 t \quad (2)$$

$$t/Q_t = t/Q_e + 1/(K_2 Q_e^2) \quad (3)$$

$$Q_t = K_1 t^{1/2} + C \quad (4)$$

$Q_e$  and  $Q_t$  are the dye adsorption amount (mg/g) at equilibrium and time  $t$ , respectively.  $K_1$  and  $K_2$  are pseudo-first-order constant and pseudo-second-order constant, respectively.  $K_1$  (mg/g•min<sup>1/2</sup>) and  $C$  (mg/g) are intra-particle diffusion rate constant and intercept, respectively.

The Langmuir and Freundlich models were utilized in the investigation of adsorption isotherms (Eqs. 5 and 6) [17].

$$C_e/Q_e = C_e/Q_m + 1/Q_m K_L \quad (5)$$

$$\ln Q_e = \ln K_F + (\ln C_e)/n \quad (6)$$

$C_e$  is the equilibrium dye concentration (mg/L).  $Q_e$  and  $Q_m$  are the equilibrium dye adsorption amount (mg/g) and the maximum dye adsorption amount (mg/g), respectively.  $K_L$  and  $K_F$  are the Langmuir and Freundlich constants (L/mg), respectively.  $n$  is an exponential parameter.

To understand the energy changes pertaining to the adsorption process, the dye adsorption on DRA was investigated by the following equations [19].

$$K = (C_0 - C_e)V/mC_e \quad (7)$$

$$\ln K = \Delta S/R - \Delta H/RT \quad (8)$$

$$\Delta G = \Delta H - T\Delta S \quad (9)$$

where  $C_0$  and  $C_e$  are the starting dye concentration (mg/L) and the equilibrium dye concentration (mg/L), respectively.  $V$  is the dye solution volume (mL), and  $m$  is the adsorbent mass (mg).  $T$  and  $R$  are the absolute temperature (K) and the gas constant, respectively.  $K$  is the thermodynamic equilibrium constant.  $\Delta S$  is the entropy difference,  $\Delta H$  is the enthalpy difference and  $\Delta G$  is the Gibbs free energy difference.

## 3 Results and discussion

### 3.1 Effect of preparation process

#### 3.1.1 Effect of reduction temperature

In this experiment, with the concentration of DETA was 20 μL/mL, RGH was prepared at the reduction temperature ranging from 65 to 95 °C. As shown in Fig. 2a, RGH can be formed with different reduction temperatures. Especially, the volume of RGHs becomes remarkably smaller when the reduction temperature is above 75 °C. This

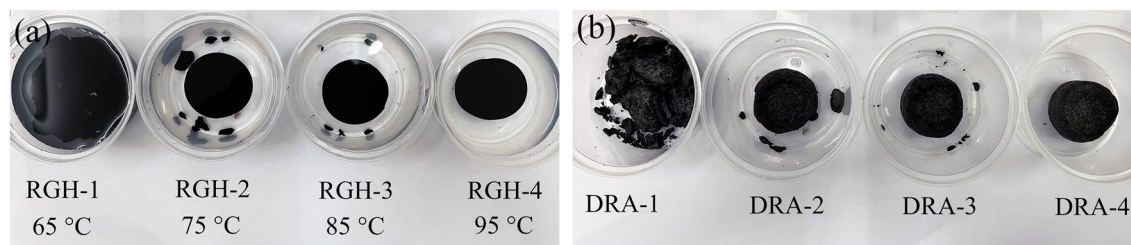


**Fig. 2** a RGHs prepared at different reduction temperatures, b Corresponding DRAs

**Fig. 3** a RGHs prepared with different DETA concentrations, b Corresponding DRAs

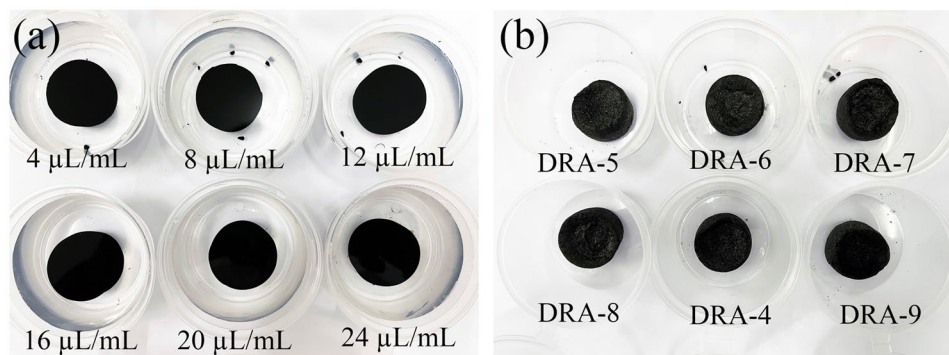


**Table 1** Density of different DRAs

Sample	Reduction temperature (°C)	DETA (μL/mL)	Density (mg/cm <sup>3</sup> )
DRA-1	65	20	/
DRA-2	75	20	9.81
DRA-3	85	20	10.48
DRA-4	95	20	11.58
DRA-5	95	4	13.24
DRA-6	95	8	12.75
DRA-7	95	12	12.01
DRA-8	95	16	11.15
DRA-9	95	24	12.14

phenomenon indicates that the self-assembly and agglomeration of the RGH are enhanced with increasing reduction temperature. After freeze drying, DRA-1 is too weak and broken, while DRA-2, DRA-3, and DRA-4 still keep the 3D structure (Fig. 2b). It shows that the increase in reduction temperature is helpful to improving the mechanical strength of DRA. Besides, from Table 1, it can be found that the density of DRA gets larger slightly with increasing reduction temperature. The result can be ascribed to the increased reduction temperature resulting in the porous structure shrinkage of DRA [20]. It is worth mentioning

that RGH-4 and DRA-4 have intact structure and higher strength compared to other samples. Thus, the effective reduction temperature of RGH is 95 °C in the experiment.

### 3.1.2 Effect of DETA concentration

To further evaluate the effect of DETA concentration on the samples, different RGHs and DRAs were prepared respectively, when the DETA concentration changes from 4 to 24 μL/mL and the reduction temperature is 95 °C. From Fig. 3; Table 1, all RGHs and DRAs possess an intact structure and better strength, while the density of DRAs changed significantly. Especially, the density of DRA-8 was as low as 11.15 mg/cm<sup>3</sup> when DETA concentration is 16 μL/mL. In this process, at a lower concentration of DETA, DETA cannot effectively cross-link the reduced GO nanosheets, so these nanosheets will spontaneously aggregate and lead to the bulk shrinkage of DRA and a higher density. However, more DETA will also lead to an increase in density (as listed in Table 1), because DETA will occupy the pores inside the aerogel material [21]. The result demonstrates that appropriately increasing the DETA concentration can effectively prevent the agglomeration of GO sheets and the collapse of the 3D porous structure of DRA. DRA-8 is thus given the fantastic property of low density. Based on the above-mentioned outcomes, DRA-8 is chosen for the subsequent adsorption study.

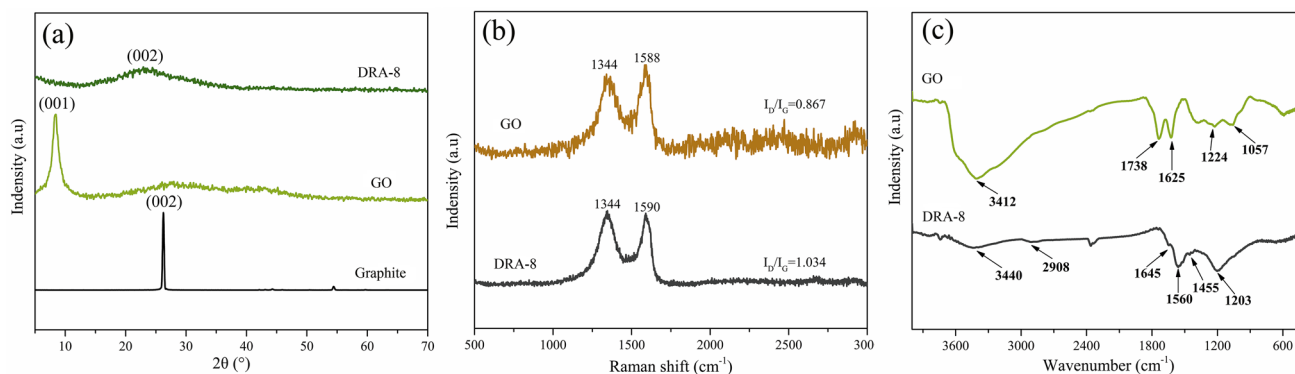


**Fig. 4** a XRD patterns of graphite, GO and DRA-8, b Raman spectra of GO and DRA-8, c FTIR spectra of GO and DRA-8

### 3.2 Characterization of DRA-8

As shown in Fig. 4a, graphite has a high characteristic peak at  $26.2^\circ$  with a layer-to-layer distance of 0.34 nm. GO prepared in this study possesses the characteristic peak at  $8.44^\circ$  with a layer-to-layer distance of 1.05 nm, indicating that graphite has been fully oxidized by the modified Hummers method. However, the DRA-8 displays a wide diffraction peak at  $22.9^\circ$ , with a layer-to-layer distance of 0.38 nm, indicating that oxygen-containing functional groups of GO are almost completely removed due to the chemical reduction [22–24].

As shown in Fig. 4b, the D and G peaks at  $1344$  and  $1590\text{ cm}^{-1}$  of GO and DRA-8 correspond to the defects and the  $\text{sp}^2$  carbon-carbon bonds, respectively. However, the  $I_D/I_G$  value of DRA-8 is 1.034, which is higher than 0.867 of GO. It demonstrates the introduction of DETA is helpful to enrich the defect density in the carbon structure [25].

From Fig. 4c, GO contains several peaks at  $3412\text{ cm}^{-1}$ ,  $1738\text{ cm}^{-1}$ ,  $1625\text{ cm}^{-1}$ ,  $1224\text{ cm}^{-1}$ , and  $1057\text{ cm}^{-1}$ , corresponding to the O–H, C=O, C=C, C–O, and C–O–C groups, respectively. To DRA-8, the peaks at  $1738$  and  $1057\text{ cm}^{-1}$  are hardly seen. It indicates that GO has been successfully reduced by DETA. This is in agreement with the result of the XRD investigation. Meantime, the new peaks at  $1560$  and  $1455\text{ cm}^{-1}$  belong to N–H and C–N in amides, respectively [26, 27]. Furthermore, the O–H stretching vibration of  $3440\text{ cm}^{-1}$  is weakened and the  $-\text{CH}_2$  of DETA molecule appears at  $2908\text{ cm}^{-1}$ . All the above information indicates that the amidation reaction occurs between GO and DETA.

Figure 5a and b display the morphology of DRA-8. It shows that the interior of DRA-8 is a three-dimensional interconnected porous network, which formed by self-assembling of reduced GO nanosheets. Meantime, DRA-8 has abundant macro-pores between 10 and  $100\text{ }\mu\text{m}$  in size. The main reason for the formation of the porous structure is

that the massive ice crystals formed inside increase the distance between the reduced GO nanosheets when RGH is frozen. During vacuum drying, all the ice crystals are detached from RGH, leaving a fluffy porous sponge structure [28, 29]. More importantly, the continuous porous structure of the DRA-8 is favorable for its adsorption capacity for dyes.

As Fig. 5c shows, DRA-8 can support a static load of at least 120 g, about 1200 times of its own weight without collapsing. Furthermore, after the static load, DRA-8 can recover its original shape without deformation. The phenomena reveal DRA-8 has excellent mechanical strength and flexibility.

### 3.3 Adsorption performance

#### 3.3.1 Effect of pH

The pH regulates the surface charge characteristics of the adsorbent and thus becomes one of the major features influencing its adsorption capability [30].

Given that the relationship between Zeta potentials and pH as shown in Fig. 6a, the surface of GO is always negatively charged in the pH range of 2–10, which is beneficial to enhance its ability to adsorb cations through electrostatic attraction. While the absolute value of Zeta potential of DRA-8 is lower than that of GO, and the isoelectric point of DRA-8 is located at pH of 3.3. In the reduction process, the positively charged amino group of DETA will react with the negatively charged epoxy and carboxyl groups of GO, resulting in the decrease of the negative charge amount of DRA-8. It can also be confirmed by the FTIR result (as shown in Fig. 4c). Consequently, the isoelectric point of DRA-8 is changed and located at pH of 3.3, and the absolute value of the Zeta potential is lower than that of GO. In fact, when the pH is below 3.3, the surface of DRA-8 is ready to accept  $\text{H}^+$  and form positively charged, facilitating its interaction with anions through electrostatic attraction. On the contrary, the

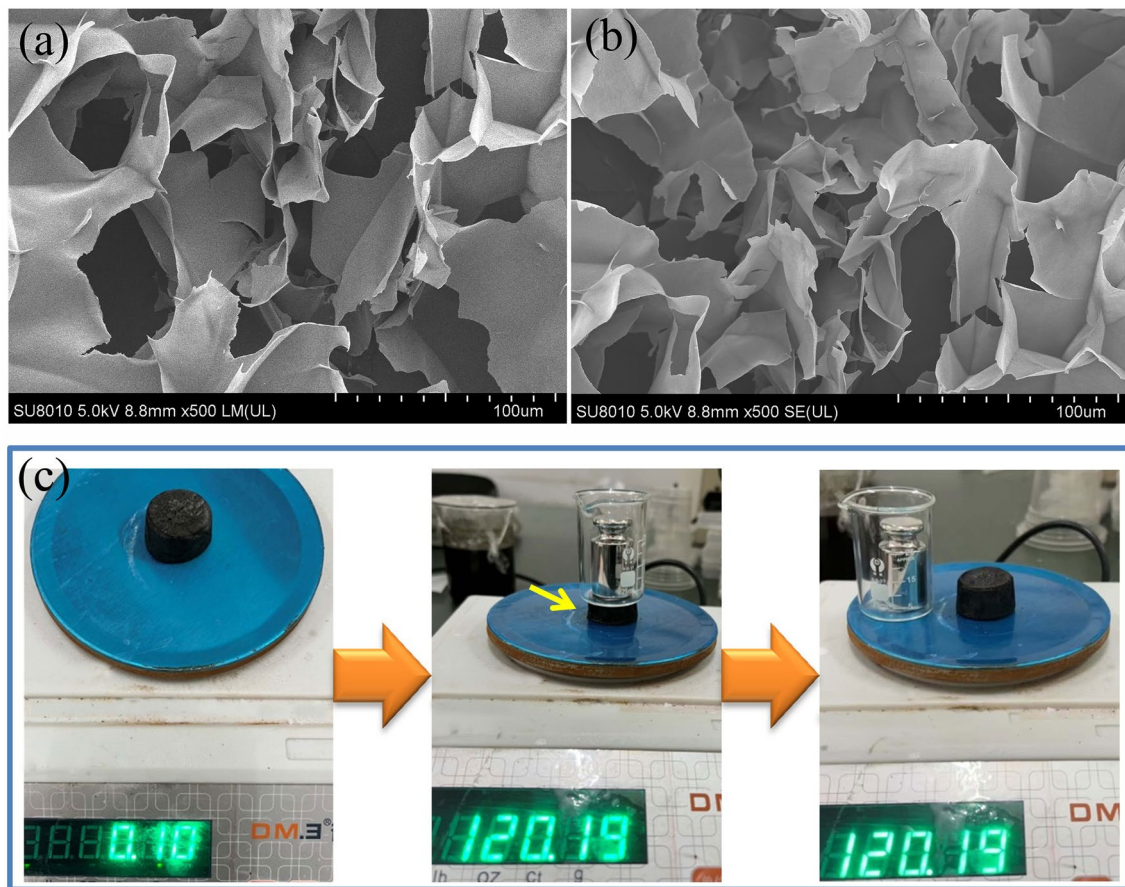


**Fig. 5** **a** and **b** SEM images and **c** photographs of the mechanical properties of DRA-8

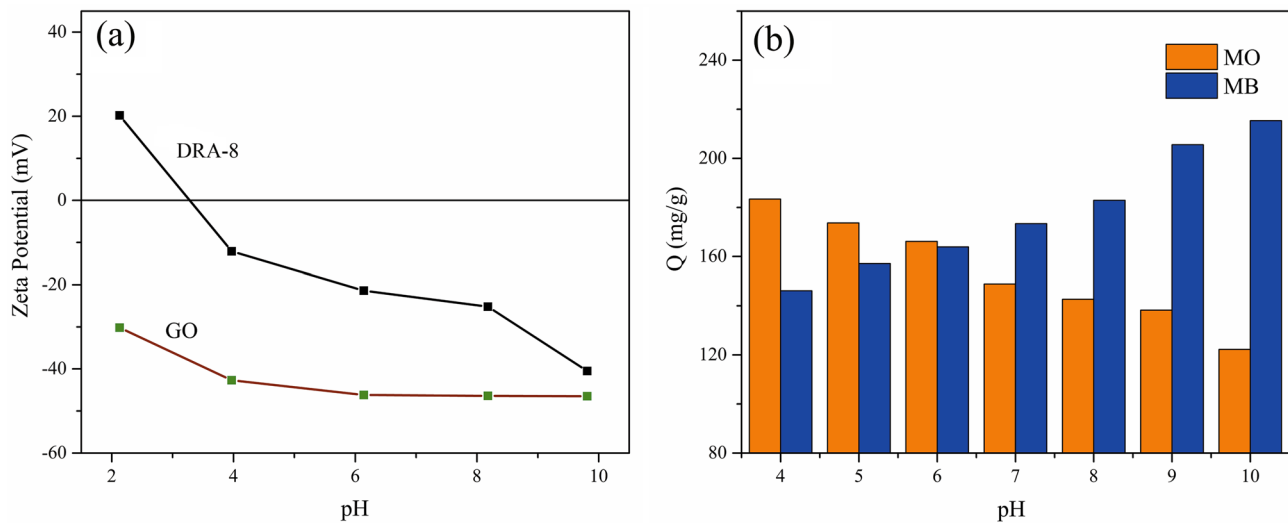


**Fig. 6** **a** Zeta potentials of GO and DRA-8, **b** Effect of pH on the MB and MO adsorption capacities of DRA-8

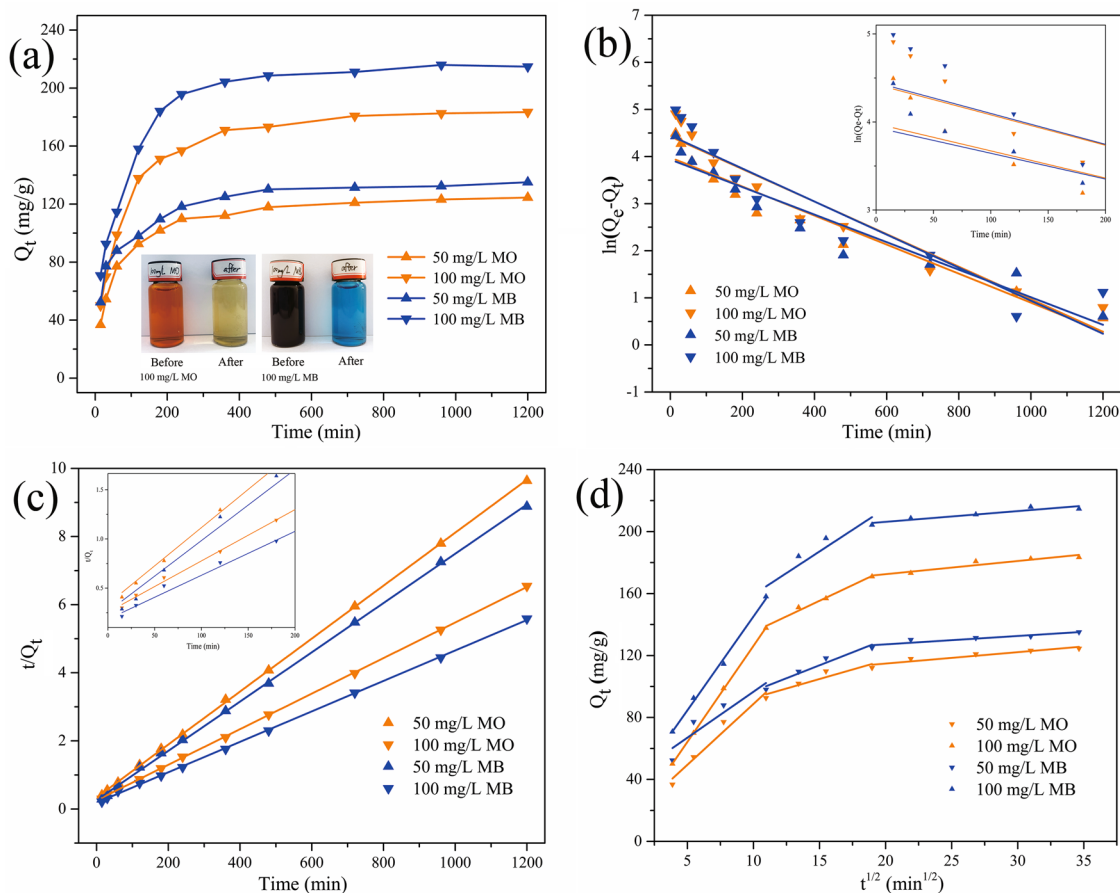


**Fig. 7** **a** Effect of contact time on the MB and MO adsorption capacity of DRA-8, **b** Pseudo-first-order model, **c** Pseudo-second-order model, and **d** Intra-particle diffusion model

pH value higher than 3.3 would lead to deprotonating and form negatively charged on the DRA-8 surface, making it easier to adsorb cations. The results indicate that the as-prepared DRA-8 has different surface charge characteristics from GO after functionalization and reduction with DETA.

Considering the importance of pH, it is crucial to explore the effect of pH on dye adsorption capacity. To achieve this aim, batches of different dye adsorption experiments were performed with the pH value changed from 4 to 10. From Fig. 6b, the adsorption capacity of anionic MO declines with raising pH, whereas the adsorption capacity of cationic MB is the opposite. This behavior is primarily due to the electrostatic behavior between DRA-8 and dye. The surface charge of DRA-8 is pH-dependent as shown in Fig. 6a, the as-prepared DRA-8 will provide a strong electrostatic attraction toward anionic MO and cationic MB, thus guaranteeing the different adsorption capacities in acidic and alkaline conditions, respectively. Consequently, DRA-8 has an excellent

adsorption capacity for MO and MB when pH is 4 and 10, respectively.

### 3.3.2 Adsorption kinetics analysis

As shown in Fig. 7a, when MO and MB concentrations are 50 mg/L, the adsorption capacity increases rapidly within 180 min and the equilibrium of adsorption is attained after 360 min. When MO and MB concentrations are 100 mg/L, the adsorption capacity enhances quickly within 240 min, and basically achieves the adsorption equilibrium at 480 min. A high adsorption rate of MO and MB from the solution can be noticed in the initial stage, which is attributed to the numerous adsorption sites on the DRA-8 owing to its superior porous structure [31].

Furthermore, the fitting of different models was done to better comprehend the adsorption kinetics mechanism. From Fig. 7b and c, and Table 2, the pseudo-second-order

**Table 2** Parameters of kinetic models of DRA for MB and MO adsorption

Dye	C <sub>0</sub> (mg/L)	Pseudo-first-order			Pseudo-second-order		
		K <sub>1</sub>	Q <sub>e</sub> (mg/g)	R <sup>2</sup>	K <sub>2</sub>	Q <sub>e</sub> (mg/g)	R <sup>2</sup>
MO	50	0.00308	53.511	0.9376	0.000179	128.62	0.99988
	100	0.00346	83.623	0.9334	0.000107	191.55	0.99986
MB	50	0.00292	51.255	0.9176	0.000201	138.24	0.99953
	100	0.00351	85.432	0.8787	0.000109	223.64	0.99958

**Table 3** Parameters of intra-particle diffusion model for MB and MO adsorption

Dye	C <sub>0</sub> (mg/L)	K <sub>i1</sub>	C <sub>1</sub>	R <sup>2</sup>	K <sub>i2</sub>	C <sub>2</sub>	R <sup>2</sup>	K <sub>i3</sub>	C <sub>3</sub>	R <sup>2</sup>
MO	50	7.86	10.11	0.9635	2.45	68.10	0.8841	0.74	100.08	0.9078
	100	12.40	2.18	0.9999	4.03	94.84	0.9887	0.85	155.48	0.9224
MB	50	5.93	37.27	0.8639	3.35	63.48	0.9542	0.54	116.40	0.8642
	100	12.12	23.99	0.9959	5.59	103.39	0.8887	0.69	192.40	0.8908

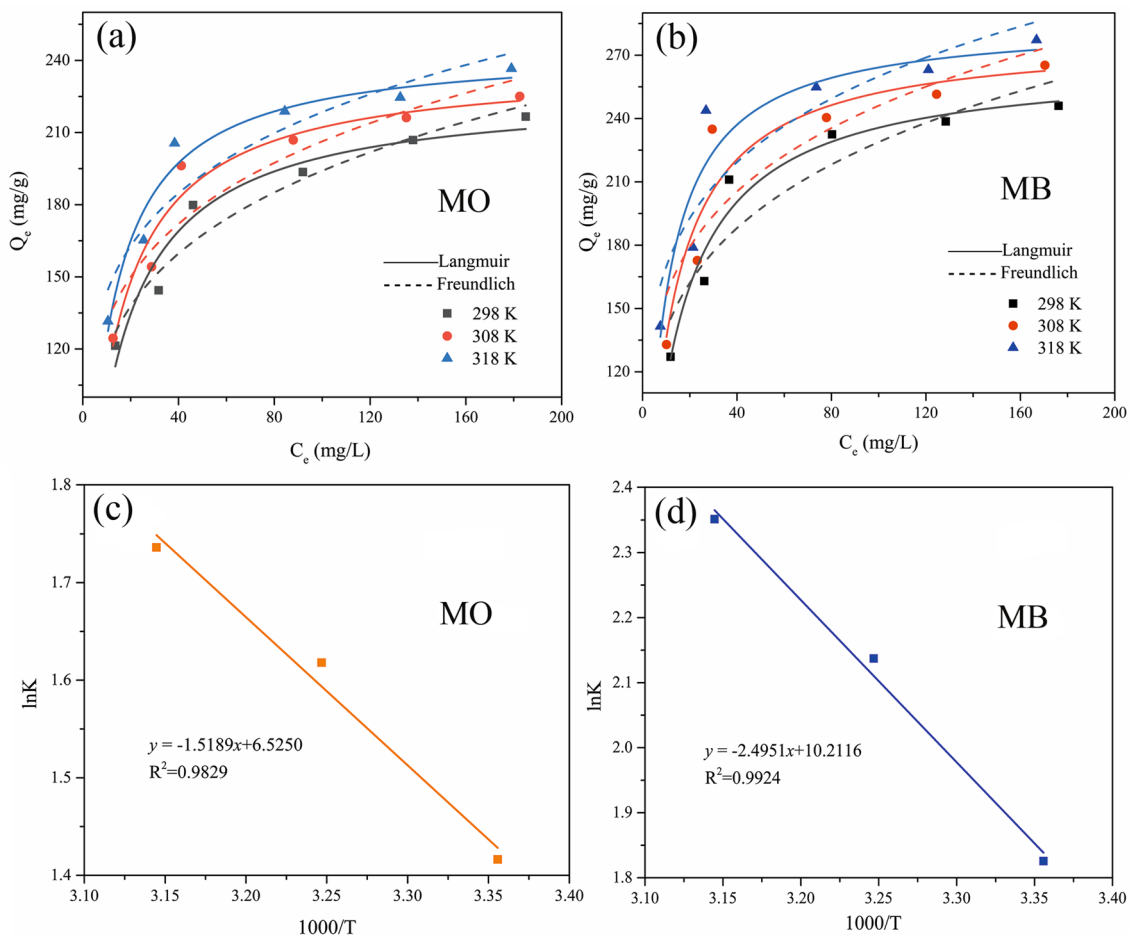


**Fig. 8** Adsorption isotherms for (a) MO and (b) MB, and thermodynamic study of (c) MO and (d) MB adsorption



model has a higher correlation coefficient ( $R^2 > 0.99$ ) than the pseudo-first-order model, suggesting that it is more appropriate for MO and MB adsorption on DRA-8.

The fitting results of the intra-particle diffusion model are shown in Fig. 7d, and the corresponding adsorption rate constants are listed in Table 3. It can be observed that the adsorption procedure can be divided into three distinct stages. The rapid surface adsorption occurs in the first stage, and the second stage involves gradual surface adsorption, with  $K_{i2}$  being less than  $K_{i1}$ . In the third stage, the adsorption tends toward equilibrium. The findings confirm that the adsorption is a multi-step process and that there are other mechanisms besides intra-particle diffusion that can regulate the adsorption [32, 33].

### 3.3.3 Adsorption isotherms analysis

Adsorption isotherms are employed to investigate adsorption mechanisms, explore the adsorbent's surface properties, and analyze the attraction between its surface and the adsorbate. In this work, the adsorption data of MO and MB on DRA-8 with different concentrations and temperatures are evaluated using the different isotherm models developed by Langmuir and Freundlich, respectively, to comprehend the corresponding mechanism. Figure 8a and b show the relevant fitted results for MO and MB adsorption, respectively. Table 4 provides the isotherm constants and resulting parameters for the different models. It can be seen that  $R_L^2$  of Langmuir isotherm model for both MO and MB is larger than  $R_F^2$  of Freundlich isotherm model, revealing that the dye adsorption of DRA-8 better fits this model. It manifests that MO and MB adsorption on DRA-8 is monolayer adsorption [34].

According to the Langmuir isotherm model, at 298, 308, and 318 K, the adsorption capacities of DRA-8 for MO are as high as 227.24 mg/g, 238.07 mg/g, and 245.44 mg/g, respectively. While the adsorption capacities of DRA-8 for MB are as high as 266.82 mg/g, 278.82 mg/g, and 286.02 mg/g, respectively. The data are superior to earlier studies [11, 30, 35–39].

### 3.3.4 Adsorption thermodynamics analysis

To investigate the thermodynamics underlying the MO and MB adsorption on DRA-8, the thermodynamic parameters were evaluated and displayed in Table 5. According to Fig. 8c and d; Table 6, the negative value of  $\Delta G$  and positive  $\Delta S$  value in the adsorption process at different temperatures, revealing the adsorption is a spontaneous thermodynamic reaction [40]. In addition, the absolute value of  $\Delta G$  increases

with temperature and the positive  $\Delta H$  value, indicating the adsorption is an endothermic process. Hence, a higher temperature is more beneficial to enhance the dye adsorption of DRA-8.

## 3.4 Adsorption mechanism

As shown in Fig. 9a, the peaks at 1112 and 1025  $\text{cm}^{-1}$  of MO/DRA-8 relate to the S=O symmetrical stretching vibration and the  $-\text{SO}_3^-$  symmetrical stretching vibration, respectively, which confirms the successful adsorption of MO on DRA-8 [41, 42]. The peaks at 1379, 1320, and 878  $\text{cm}^{-1}$  of MB/DRA-8, belonging to the stretching vibration of C–N, symmetric deformation vibrations of  $-\text{CH}_3$ , and rocking vibration of aromatic rings in MB, which reveal the successful adsorption of MB on DRA-8 [43, 44]. The peaks of C=C groups in MB/DRA-8 and MO/DRA-8 are shifted from 1560 to 1549 and 1541  $\text{cm}^{-1}$ , respectively, which is attributed to the  $\pi$  electron interaction in the aromatic ring as  $\pi$ – $\pi$  interaction [45].

According to Fig. 6a, DRA-8 has a negative surface charge when the pH value exceeds 3.3. As a cationic dye, the positive surface charge of MB is beneficial to increase its electrostatic attraction with the negatively charged DRA-8. Simultaneously, DRA-8 also connects with MB through  $\pi$ – $\pi$  interaction, thereby enhancing its adsorption capacity. While for anionic MO, electrostatic repulsion is formed between DRA-8 and MO due to its negatively charged surface. As a result, the adsorption capacity of the DRA-8 to MO mainly depends on the  $\pi$ – $\pi$  interaction. Figure 9b shows the corresponding mechanism of MO and MB adsorption on DRA-8.

To clearly understand the adsorption capacity advantage of the synthesized DRA-8, the adsorption capacity comparison of different adsorbents is displayed in Table 6. From Table 6, it is evident that the DRA-8 is a more competitive adsorbent for the successful elimination of MO and MB from dye wastewater.

**Table 5** Thermodynamic parameters of adsorption of MO and MB on DRA-8

Dye	T(K)	$\Delta G$ (kJ/mol)	$\Delta H$ (kJ/mol)	$\Delta S$ (kJ/mol/K)
MO	298	–3.5091	12.6278	0.0542
	308	–4.1435		
	318	–4.5901		
MB	298	–4.5234	20.7447	0.0849
	308	–5.4724		
	318	–6.2169		

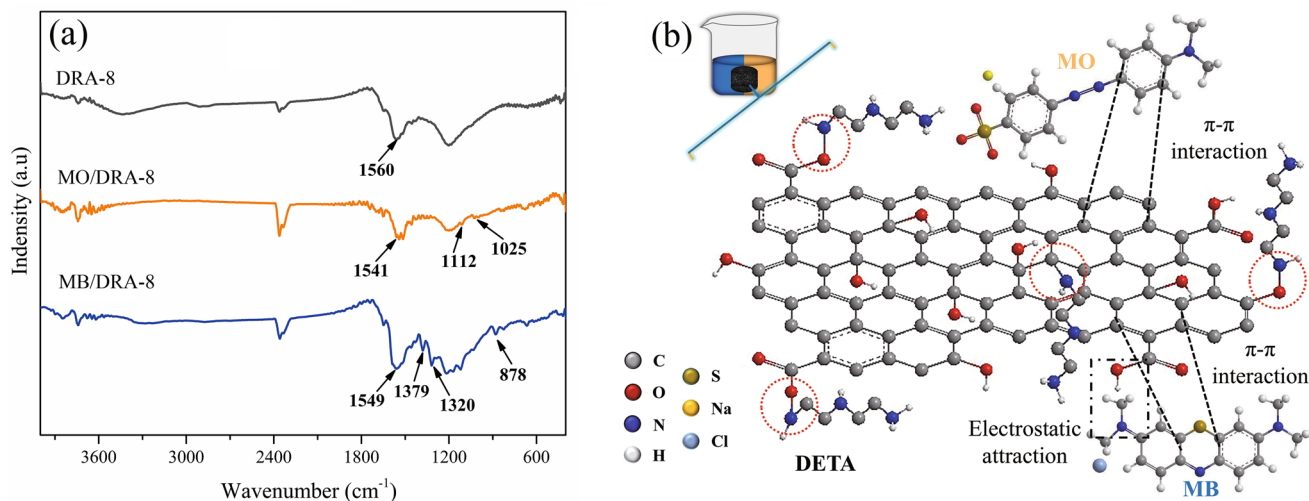


**Fig. 9** a FTIR spectra of DRA-8 before and after MO and MB adsorption, b Mechanism of MO and MB adsorption of DRA-8

**Table 4** Parameters of different isotherm models for MB and MO adsorption

Dye	T(K)	Langmuir			Freundlich		
		$K_L$	$Q_m(\text{mg/g})$	$R_L^2$	$K_F$	$n$	$R_F^2$
MO	298	0.0726	227.24	0.9515	72.78	4.694	0.9489
	308	0.0821	238.07	0.9547	82.84	5.046	0.8917
	318	0.1027	245.44	0.9639	94.13	5.469	0.9006
MB	298	0.0756	266.82	0.9604	85.41	4.672	0.8725
	308	0.0948	278.82	0.9028	99.22	5.070	0.8096
	318	0.1210	286.02	0.9002	110.68	5.393	0.8309

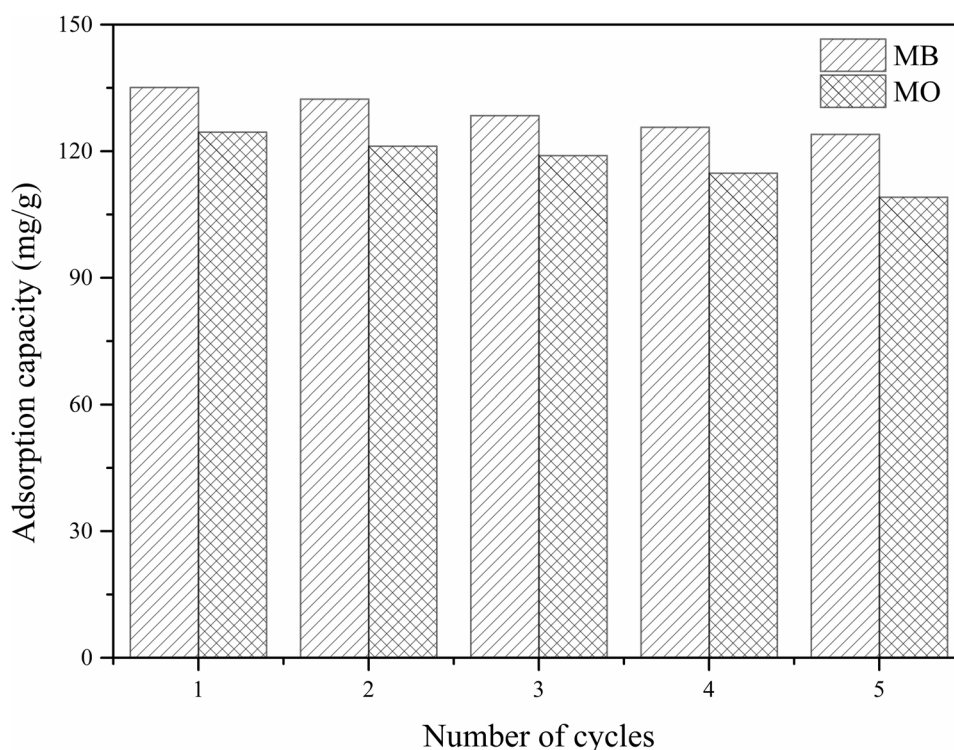
**Table 6** Comparison of the adsorption capacities of different adsorbents

Dye	Adsorbents	Adsorption capacity (mg/g)	References
MO	CS/GO	38.67	[35]
	h-MoS <sub>2</sub>	41.52	[36]
	APSP	143.70	[37]
	GA	166.67	[11]
	DRA-8	227.24	This work
MB	PVA/PCMC/GO	89.29	[30]
	GO-MMT/SA	150.66	[38]
	CMC/GOCOOH	180.23	[39]
	GA	221.74	[11]
	DRA-8	266.82	This work

### 3.5 Reusability experiments

In addition to the absorption capacity, the reusability is an important index for the practical application of DRA-8. In this work, to assess the reusability of the DRA-8, it was subjected to multiple adsorption-desorption experiments. After each adsorption, DRA-8 containing dye was immersed into 0.1 M NaOH (or HCl) solution and washed with deionized water until neutral to obtain regenerated material. The recovered DRA-8 was then reused in the next adsorption cycle. This process was repeated 5 times and the results are shown in Fig. 10. It can be observed that DRA-8 can keep a high adsorption capacity for MB and MO with a tiny loss after 5 cycles. The result indicates DRA-8 has extraordinary reusability and great application potential for dye adsorption.

**Fig. 10** Reusability of DRA-8 for MB and MO after different numbers of cycles



## 4 Conclusion

The low-density DRA-8 was effectively synthesized with a reduction temperature of 95 °C and a DETA concentration of 16  $\mu\text{L/mL}$ . Through the microstructural characterization, DRA-8 exhibits a three-dimensional interconnected porous network with numerous macropores ranging in size from 10 to 100  $\mu\text{m}$ . The experimental results show the adsorption process is suitable with the pseudo-second-order model and spontaneous thermodynamic reaction. The adsorption mechanism reveals that the cationic MB adsorption is mainly related to  $\pi$ - $\pi$  interaction and electrostatic attraction. Nevertheless, for anionic MO, the adsorption capacity mainly depends on  $\pi$ - $\pi$  interactions. Furthermore, DRA-8 demonstrates a good regeneration performance for MB and MO adsorptions.

**Acknowledgements** The authors gratefully acknowledge the support of this research by the National Natural Science Foundation of China (Grant No. 52062021), the Natural Science Foundation of Jiangxi Province of China (Grant No. 20212BAB204034) and the Key Foundation of Jiangxi Educational Committee (Grant No. GJJ211302).

**Author contributions** LJ wrote the main manuscript text, LJ, BY, ZY and CL performed the experiments, XH supervised the process. All authors reviewed the manuscript.

## Declarations

**Conflict of interest** The authors declare no conflict of interest concerning in the present study.

## References

1. M. Hasanpour, M. Hatami, Photocatalytic performance of aerogels for organic dyes removal from wastewaters: review study[J]. *J. Mol. Liq.* **309**, 113094 (2020). <https://doi.org/10.1016/j.molliq.2020.113094>
2. S. Venkatesan, Y.Y. Chen, H. Teng et al., Enhanced adsorption on  $\text{TiO}_2$  photoelectrodes of dye-sensitized solar cells by electrochemical methods dye[J]. *J. Alloys Compd.* **903**, 163959 (2022). <https://doi.org/10.1016/j.jallcom.2022.163959>
3. P.V. Vu, T.D. Doan, G.C. Tu et al., A novel application of cellulose aerogel composites from pineapple leaf fibers and cotton waste: removal of dyes and oil in wastewater[J]. *J. Porous Mater.* **29**, 1137–1147 (2022). <https://doi.org/10.1007/s10934-022-01238-w>
4. S. Velusamy, A. Roy, S. Sundaram et al., A review on heavy metal ions and containing dyes removal through graphene oxide-based adsorption strategies for textile wastewater treatment[J]. *Chem. Record.* **21**(7), 1570–1610 (2021). <https://doi.org/10.1002/tcr.202000153>
5. C. Zhang, N. Qin, A. Pan et al., Hollow  $\text{Fe}_2\text{O}_3$  nanotubes derived from metal-organic framework for enhanced lithium storage and dye adsorption[J]. *J. Porous Mater.* **28**(3), 673–681 (2021). <https://doi.org/10.1007/s10934-020-01019-3>
6. F.E. Che Othman, M.S. Ismail, N. Yusof et al., Methane adsorption by porous graphene derived from rice husk ashes under various stabilization temperatures[J]. *Carbon Lett.* **30**(5), 535–543 (2020). <https://doi.org/10.1007/s42823-020-00123-3>
7. T.H. Tu, P.T.N. Cam, M.T. Phong et al., Synthesis and application of graphene oxide aerogel as an adsorbent for removal of dyes from water[J]. *Mater. Lett.* **238**, 134–137 (2019). <https://doi.org/10.1016/j.matlet.2018.11.164>
8. M. Han, B. Xu, M. Zhang et al., Preparation of biologically reduced graphene oxide-based aerogel and its application in dye

- adsorption[J]. *Sci. Total Environ.* **783**, 147028 (2021). <https://doi.org/10.1016/j.scitotenv.2021.147028>
9. G.Z. Kyzas, E.A. Deliyanni, K.A. Matis, Graphene oxide and its application as an adsorbent for wastewater treatment[J]. *J. Chem. Technol. Biotechnol.* **89**(2), 196–205 (2014). <https://doi.org/10.1002/jctb.4220>
  10. D.K. Singh, V. Kumar, S. Mohan et al., Polylysine functionalized graphene aerogel for the enhanced removal of Cr(VI) through adsorption: kinetic, isotherm, and thermodynamic modeling of the process[J]. *J. Chem. Eng. Data* **62**(5), 1732–1742 (2017). <https://doi.org/10.1021/acs.jced.7b00188>
  11. T. Trinh, T.H. T P N X, Quan, T.N.M. Anh et al., Preparing three-dimensional graphene aerogels by chemical reducing method: investigation of synthesis condition and optimization of adsorption capacity of organic dye[J]. *Surf. Interfaces* **23**, 101023 (2021). <https://doi.org/10.1016/j.surfin.2021.101023>
  12. C. Chen, X. Zhu, B. Chen, Covalently cross-linked graphene oxide aerogel with stable structure for high-efficiency water purification[J]. *Chem. Eng. J.* **354**, 896–904 (2018). <https://doi.org/10.1016/j.cej.2018.08.034>
  13. S. Tang, D. Xia, Y. Yao et al., Dye adsorption by self-recoverable, adjustable amphiphilic graphene aerogel[J]. *J. Colloid Interface Sci.* **554**, 682–691 (2019). <https://doi.org/10.1016/j.jcis.2019.07.041>
  14. X. Hu, Y. Yu, Y. Wang et al., Separating nano graphene oxide from the residual strong-acid filtrate of the modified Hummers method with alkaline solution[J]. *Appl. Surf. Sci.* **329**, 83–86 (2015). <https://doi.org/10.1016/j.apsusc.2014.12.110>
  15. C. Gao, Z. Dong, X. Hao et al., Preparation of reduced graphene oxide aerogel and its adsorption for Pb(II)[J]. *ACS Omega* **5**(17), 9903–9911 (2020). <https://doi.org/10.1021/acsomega.0c00183>
  16. X. Wang, Y. Guo, Z. Jia et al., Fabrication of graphene oxide/polydopamine adsorptive membrane by stepwise in-situ growth for removal of rhodamine B from water[J]. *Desalination* **516**, 115220 (2021). <https://doi.org/10.1016/j.desal.2021.115220>
  17. S. Nundy, A. Ghosh, R. Nath et al., Reduced graphene oxide (rGO) aerogel: efficient adsorbent for the elimination of antimony (III) and (V) from wastewater[J]. *J. Hazard. Mater.* **420**, 126554 (2021). <https://doi.org/10.1016/j.jhazmat.2021.126554>
  18. Y. Önal, C. Akmil-Başar, D. Eren et al., Adsorption kinetics of malachite green onto activated carbon prepared from Tunçbilek lignite[J]. *J. Hazard. Mater.* **128**(2–3), 150–157 (2006). <https://doi.org/10.1016/j.jhazmat.2005.07.055>
  19. D. Wang, L. Liu, X. Jiang et al., Adsorbent for p-phenylenediamine adsorption and removal based on graphene oxide functionalized with magnetic cyclodextrin[J]. *Appl. Surf. Sci.* **329**, 197–205 (2015). <https://doi.org/10.1016/j.apsusc.2014.12.161>
  20. L. Li, B. Li, J. Zhang, Dopamine-mediated fabrication of ultralight graphene aerogels with low volume shrinkage[J]. *J. Mater. Chem. A* **4**(2), 512–518 (2016). <https://doi.org/10.1039/C5TA08829A>
  21. T. Trinh, D.T. T P N X, Quang, T.H. Tu et al., Fabrication, characterization, and adsorption capacity for cadmium ions of graphene aerogels[J]. *Synth. Met.* **247**, 116–123 (2019). <https://doi.org/10.1016/j.synthmet.2018.11.020>
  22. V.A. Nebol'sin, V. Galstyan, Y.E. Silina, Graphene oxide and its chemical nature: multi-stage interactions between the oxygen and graphene[J]. *Surf. Interfaces* **21**, 100763 (2020). <https://doi.org/10.1016/j.surfin.2020.100763>
  23. P. Bradder, S.K. Ling, S. Wang et al., Dye adsorption on layered graphite oxide[J]. *J. Chem. Eng. Data* **56**(1), 138–141 (2011). <https://doi.org/10.1021/je101049g>
  24. P. Tan, J. Sun, Y. Hu et al., Adsorption of Cu<sup>2+</sup>, Cd<sup>2+</sup> and Ni<sup>2+</sup> from aqueous single metal solutions on graphene oxide membranes[J]. *J. Hazard. Mater.* **297**, 251–260 (2015). <https://doi.org/10.1016/j.jhazmat.2015.04.068>
  25. Y. Luan, H. Zhang, F. Yang et al., Rational design of NiCo<sub>2</sub>S<sub>4</sub> nanoparticles@N-doped CNT for hybrid supercapacitor[J]. *Appl. Surf. Sci.* **447**, 165–172 (2018). <https://doi.org/10.1016/j.apsusc.2018.03.236>
  26. J.H. Kang, J.S. Chen, Using ethylenediamine to prepare three dimensional nitrogen-doped graphene aerogel/sulfur composite for lithium–sulfur batteries[J]. *Diam. Relat. Mater.* **88**, 222–229 (2018). <https://doi.org/10.1016/j.diamond.2018.07.015>
  27. L. Jiang, Y. Wen, Z. Zhu et al., A double cross-linked strategy to construct graphene aerogels with highly efficient methylene blue adsorption performance[J]. *Chemosphere* **265**, 129169 (2021). <https://doi.org/10.1016/j.chemosphere.2020.129169>
  28. J. Xie, L. Niu, Y. Qiao et al., The influence of the drying method on the microstructure and the compression behavior of graphene aerogel[J]. *Diam. Relat. Mater.* **121**, 108772 (2022). <https://doi.org/10.1016/j.diamond.2021.108772>
  29. J. Wu, X. Qiu, S. Chen, Preparation and characterization of an amine-modified graphene aerogel for enhanced carbon dioxide adsorption[J]. *J. Mater. Sci.* **57**(3), 1727–1737 (2022). <https://doi.org/10.1007/s10853-021-06768-3>
  30. H. Dai, Y. Huang, H. Huang, Eco-friendly polyvinyl alcohol/carboxymethyl cellulose hydrogels reinforced with graphene oxide and bentonite for enhanced adsorption of methylene blue[J]. *Carbohydr. Polym.* **185**, 1–11 (2018). <https://doi.org/10.1016/j.carbpol.2017.12.073>
  31. Q. Yang, R. Lu, S.S. Ren et al., Three dimensional reduced graphene oxide/ZIF-67 aerogel: effective removal cationic and anionic dyes from water[J]. *Chem. Eng. J.* **348**, 202–211 (2018). <https://doi.org/10.1016/j.cej.2018.04.176>
  32. G. Crini, H.N. Peindy, F. Gimbert et al., Removal of CI Basic Green 4 (Malachite Green) from aqueous solutions by adsorption using cyclodextrin-based adsorbent: kinetic and equilibrium studies[J]. *Sep. Purif. Technol.* **53**(1), 97–110 (2007). <https://doi.org/10.1016/j.seppur.2006.06.018>
  33. S. Jiang, T. Yu, R. Xia et al., Realization of super high adsorption capability of 2D δ-MnO<sub>2</sub>/GO through intra-particle diffusion[J]. *Mater. Chem. Phys.* **232**, 374–381 (2019). <https://doi.org/10.1016/j.matchemphys.2019.05.004>
  34. G. Moussavi, Z. Hossaini, M. Pourakbar, High-rate adsorption of acetaminophen from the contaminated water onto double-oxidized graphene oxide[J]. *Chem. Eng. J.* **287**, 665–673 (2016). <https://doi.org/10.1016/j.cej.2015.11.025>
  35. W. Zhu, X. Jiang, F. Liu et al., Preparation of chitosan-graphene oxide composite aerogel by hydrothermal method and its adsorption property of methyl orange[J]. *Polymers* **12**(9), 2169 (2020). <https://doi.org/10.3390/polym12092169>
  36. Y. Wu, M. Su, J. Chen et al., Superior adsorption of methyl orange by h-MoS<sub>2</sub> microspheres: Isotherm, kinetics, and thermodynamic studies[J]. *Dyes Pigm.* **170**, 107591 (2019). <https://doi.org/10.1016/j.dyepig.2019.107591>
  37. M.V. Subbaiah, D.S. Kim, Adsorption of methyl orange from aqueous solution by aminated pumpkin seed powder: kinetics, isotherms, and thermodynamic studies[J]. *Ecotoxicol. Environ. Saf.* **128**, 109–117 (2016). <https://doi.org/10.1016/j.ecoenv.2016.02.016>
  38. E. Tao, D. Ma, S. Yang et al., Graphene oxide-montmorillonite/sodium alginate aerogel beads for selective adsorption of methylene blue in wastewater[J]. *J. Alloys Compd.* **832**, 154833 (2020). <https://doi.org/10.1016/j.jallcom.2020.154833>
  39. A.S. Eltaweil, G.S. Elgarhy, G.M. El-Subruiti et al., Carboxymethyl cellulose/carboxylated graphene oxide composite microbeads for efficient adsorption of cationic methylene blue dye[J]. *Int. J. Biol. Macromol.* **154**, 307–318 (2020). <https://doi.org/10.1016/j.ijbiomac.2020.03.122>
  40. E.S.R.E. Hassan, M. Rostom, F.E. Farghaly et al., Bio-sorption for tannery effluent treatment using eggshell wastes; kinetics,

- isotherm and thermodynamic study[J]. *Egypt. J. Petroleum* **29**(4), 273–278 (2020). <https://doi.org/10.1016/j.ejpe.2020.10.002>
41. Y. Jiang, B. Liu, J. Xu et al., Cross-linked chitosan/ $\beta$ -cyclodextrin composite for selective removal of methyl orange: adsorption performance and mechanism[J]. *Carbohydr. Polym.* **182**, 106–114 (2018). <https://doi.org/10.1016/j.carbpol.2017.10.097>
  42. L. Deng, Z. Shi, X. Peng et al., Magnetic calcinated cobalt ferrite/magnesium aluminum hydrotalcite composite for enhanced adsorption of methyl orange[J]. *J. Alloys Compd.* **688**, 101–112 (2016). <https://doi.org/10.1016/j.jallcom.2016.06.227>
  43. M. Yan, W. Huang, Z. Li, Chitosan cross-linked graphene oxide/lignosulfonate composite aerogel for enhanced adsorption of methylene blue in water[J]. *Int. J. Biol. Macromol.* **136**, 927–935 (2019). <https://doi.org/10.1016/j.ijbiomac.2019.06.144>
  44. Z. Wu, W. Huang, X. Shan et al., Preparation of a porous graphene oxide/alkali lignin aerogel composite and its adsorption properties for methylene blue[J]. *Int. J. Biol. Macromol.* **143**, 325–333 (2020). <https://doi.org/10.1016/j.ijbiomac.2019.12.017>
  45. A.S.K. Kumar, N. Rajesh, Exploring the interesting interaction between graphene oxide, Aliquat-336 (a room temperature ionic liquid) and chromium (VI) for wastewater treatment[J]. *RSC Adv.* **3**(8), 2697–2709 (2013). <https://doi.org/10.1039/C2RA22627H>

**Publisher's Note** Springer Nature remains neutral with regard to jurisdictional claims in published maps and institutional affiliations.

Springer Nature or its licensor (e.g. a society or other partner) holds exclusive rights to this article under a publishing agreement with the author(s) or other rightsholder(s); author self-archiving of the accepted manuscript version of this article is solely governed by the terms of such publishing agreement and applicable law.